Exploiting Color Name Space for Salient Object Detection

Jing Lou, Huan Wang, Longtao Chen, Qingyuan Xia, Wei Zhu, and Mingwu Ren

arXiv:1703.08912v1 [cs.CV] 27 Mar 2017

***Abstract*—In this paper, we will investigate the contribution of color names for salient object detection. Each input image is first converted to the color name space, which is consisted of 11 probabilistic channels. By exploring the topological structure relationship between the figure and the ground, we obtain a saliency map through a linear combination of a set of sequential attention maps. To overcome the limitation of only exploiting the surroundedness cue, two global cues with respect to color names are invoked for guiding the computation of another weighted saliency map. Finally, we integrate the two saliency maps into a unified framework to infer the saliency result. In addition, an improved post-processing procedure is introduced to effectively suppress the background while uniformly highlight the salient objects. Experimental results show that the proposed model produces more accurate saliency maps and performs well against 23 saliency models in terms of three evaluation metrics on three public datasets.**

***Index Terms*—Saliency, salient object detection, figure-ground segregation, surroundedness, color names, color name space.**

I. Introduction

VISUAL attention, one of intrinsic properties of human vision to extract important information from abundant visual inputs, is concerned with the understanding and modeling of biological perception systems. Psychophysical and physiological studies indicate that the selective attention mechanism, which can be directed by the visual system of humans to gaze the currently most conspicuous parts and shift in different locations, plays an important role in the early representation [1]. Since these conspicuous parts might be prior knowledge based visual cues or feature based salient regions, computational visual attention aims to deal with the automatic saliency detection in images and videos. In computer vision, the main tasks of saliency research include eye fixation prediction which attempts to predict human fixation data [2]–[7], and salient object detection for localization and identification of salient regions in the visual scene [8]–[12].

Over the past decades, saliency detection has been widely used in many computer vision applications, including image segmentation [13], object detection [14], object recognition [15], visual tracking [16], image and video compression [17], and video summarization [18]. Generally, the resultant map for saliency detection is called "saliency map", where each value topographically describes the conspicuity of a location in the visual field. From a computational point of view, saliency detection techniques can be divided into two categories: slow, top-down, task-dependent manner; and rapid, bottom-up, task-independent manner [19]. Although top-down processes are indispensable for guiding the attention to behaviorally relevant objects, the salient features based bottom-up attention is more closely related to an early stage in the nervous system [1], [20], and has been investigated by numerous researchers.

In the feature integration theory of attention, the visual scene is initially coded along a number of elementary features, e.g., color, orientation, brightness, and spatial frequency [20]. Furthermore, the selective attention mechanism [1] suggests to compute these elementary features in parallel and combine the resultant cortical topographic maps into the saliency map. Hence, a majority of bottom-up saliency models aim to investigate different visual features and apply them to define the saliency of a pixel or a region. In these models, contrast-based detection is one of the most commonly adopted techniques. As no prior knowledge regarding salient objects is provided, contrast-based saliency models mainly focus on two aspects, i.e., local center-surround difference, and global rarity.

For the center-surround contrast, one of the most influential bottom-up saliency models is introduced by Itti et al. [2] based on the Koch and Ullman's early representation model [1]. They extract various features from the input color image at multiple resolutions, and use center-surround differences between different resolutions to form the final saliency map. Ma and Zhang [21] regard an image as a perceive field and define the saliency by measuring the differences between the stimuli perceived by different perception units. A subsequent fuzzy growing is performed to extract attended areas from saliency maps. Goferman et al. [22] base on four basic principles of human visual attention to detect context-aware saliency, i.e., local low-level features, global considerations, visual organization rules, and high-level factors. Furthermore, by means of the Kullback-Leibler divergence, an information-theoretic approach is proposed to extract saliency from the multi-scale center-surround feature distributions [23].

For another, global contrast based saliency models tend to find rare features from the entire image. Achanta et al. [8] propose a frequency-tuned approach (FT) which defines pixel-level saliency by comparing the color of each pixel with the average image color in the LAB color space. In [9], a histogram contrast based salient object detection model (HC) is presented, in which the color statistics of an input image are used to compute the saliency at each location. In addition, that paper also introduces a spatially weighted region contrast based saliency (RC). In order to reduce the complexity of calculating the color contrasts between regions, we subsequently follow the RC method and propose a regional

The authors are with the School of Computer Science and Engineering, Nanjing University of Science and Technology, Nanjing 210094, Jiangsu Province, P.R. China.

Corresponding author: M. Ren (mingwuren@163.com)

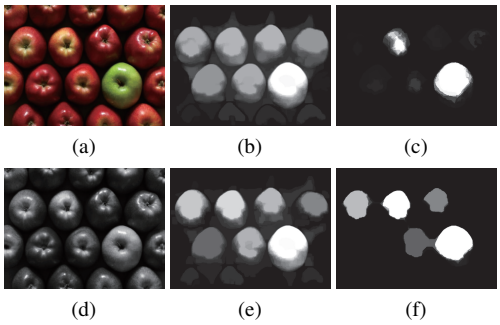

Figure 1. (a) RGB image from the ImgSal dataset [7], and its corresponding saliency maps produced by (b) BMS [5] and (c) our model. (d) Gray-scale image, and the resultant saliency maps of (e) BMS and (f) our model.

principal color based saliency method (RPC) [24] by only retaining the most frequently occurred color in each region. Besides widely used color feature, some other visual cues are also exploited in many global contrast based saliency models, such as intensity [25], spectrum [3], [7], and texture [26].

In this study, we also focus on bottom-up, contrast-based saliency approach. Actually, if we review the task of salient object detection, we can see that it has two clear implications: one is that the detected regions should be salient in the entire scene, the other is that these salient regions should contain objects of any category. Gestalt psychological studies indicate that objects lying in the foreground may result in being more salient than background elements [27], [28]. Since salient objects are more likely to be involved in foreground regions, two questions consequently arise: 1) How to extract foreground objects? 2) How to define contrast-based saliency? For the first question, one answer is to employ figure-ground segregation.

Recently, a simple and effective model called "Boolean Map based Saliency" (BMS) is proposed in [5]. This work first demonstrates that rarity based models sometimes ignore global structure information and falsely highlight high contrast regions. Then following the suggestion of Gestalt psychology that the surroundedness may influence figure-surround segregation [29], the authors exploit a set of randomly sampled boolean maps to model the saliency of a foreground object. By using different parameter settings, BMS is suitable for both eye fixation prediction and salient object detection, and achieves the state-of-the-art performance.

Here, we only discuss its results of salient object detection. Although three channels of the LAB color space are chosen as randomly sampled features maps, the essence of BMS is the use of closed outer contours of foreground objects in an image. The effect of salient object detection is somewhat equivalent to applying it to a gray-scale image. As illustrated in Fig. 1, it is interesting that if we convert the input (Fig. 1a) to a gray-scale image (Fig. 1c) and apply BMS to them respectively, we obtain two similar saliency maps (cf. Figs. 1b and 1e) in which all of the detected salient regions have the same characteristics. That is, they are enclosed by the outer boundaries and not connected to the image borders. Obviously, the color information is discarded and not considered in this case.

In this paper, we couple two global color cues and the topological structure information into a unified framework by extending the BMS model to a *Color Name Space*, which is obtained using the PLSA-bg color naming model [30] (or called PLSA-ind in [31]). In computer vision, color names are linguistic color labels assigned to image pixels. The linguistic study of Berlin and Kay [32] indicates that there are eleven basic color terms (i.e., color names) in the English language, as given in Table I. In the proposed model, both the probabilities and statistics of eleven color names are simultaneously incorporated to measure color differences. Compared with BMS, the topological information also participates in the computation of the color based saliency, hence generates several weighted master attention maps. Through a simple linear combination and an improved post-processing procedure, we obtain two kinds of saliency maps and then fuse them into a single map. Furthermore, several image processing procedures, including truncation operation and intensity transformation, are also invoked to infer the final result and refine it. Figures 1c and 1f show the saliency results produced by the proposed model. We can see that the color contrast based saliency shows higher precision, which demonstrates that the color cue is of as much importance as the surroundedness feature that used in BMS.

Table I
ELEVEN BASIC COLOR TERMS OF THE ENGLISH LANGUAGE

i	1	2	3	4	5
Term (t_i)	black	blue	brown	grey	green
RGB (c_i)	[0 0 0]	[0 0 1]	[.5 .4 .25]	[.5 .5 .5]	[0 1 0]
6	7	8	9	10	11
orange	pink	purple	red	white	yellow
[1 .8 0]	[1 .5 1]	[1 0 1]	[1 0 0]	[1 1 1]	[1 1 0]

In the following sections, the proposed saliency model will be called "CNS". The main contributions of this work include:

1. We propose an integrated model to detect salient objects by exploiting the color name space for an individual image, which computes more effective color based saliency.
2. A weighted global contrast mechanism is introduced by incorporating more color cues into the topological structure of a scene.
3. An improved post-processing procedure is proposed to uniformly highlight salient regions and smooth them, which provides an easy way for further salient object segmentation.

This paper is organized as follows: Section II is the review of related work. In Section III, we present the salient object detection model based on the color name space. In Section IV, we discuss experimental details, evaluation measures, parameter analysis, and results. Conclusions and possible extensions are presented in Section V.

II. Related Work

We base the proposed salient object detection model on BMS [5] and PLSA-bg [30]. The key idea of BMS is the surroundedness, which is characterized by a set of boolean maps. The authors first convert an input RGB image to the LAB color space, and scale each color channel to the integer range $[0, 255]$. Subsequently, they choose all three color channels of the LAB output as the input feature maps, and use a set of

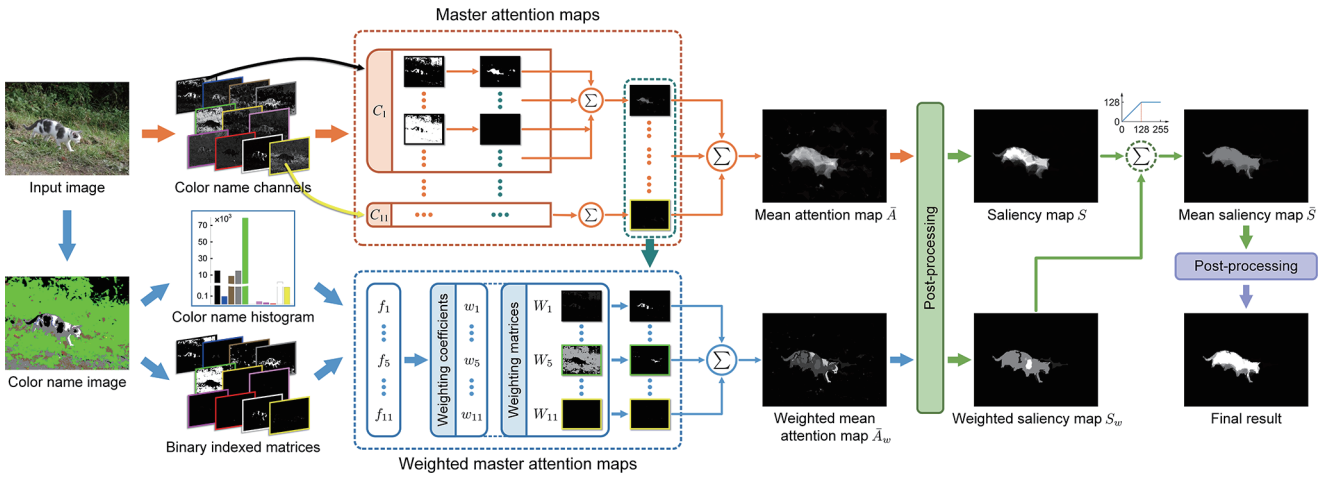

Figure 2. Framework of the proposed CNS model.

fixed thresholds to binarize each feature map to boolean maps B_i as follows [5]:

$$B_i = \texttt{THRESH}\left(\phi(I), \theta\right) . \tag{1}$$

where $\phi(I)$ is a feature map of the input I with the integer range of values $[0, 255]$, and θ represents a fixed threshold in the same range. Based on a Gestalt principle for figure-ground segregation [29], BMS then performs some morphological operations including opening and flood-fill on these boolean maps to generate a set of attention maps, in which all the regions connected to the image borders are masked out since they are not surrounded by closed outer contours. The final saliency map is simply the average of all the attention maps, followed by a morphological post-processing, including erosion, dilation, and reconstruction.

The surroundedness cue is also invoked in the proposed CNS model. However, different from BMS, our model uses the color name space instead of the LAB color space, which comes from the PLSA-bg model [30]. In the field of document analysis, the standard PLSA model computes the conditional probability of a word w in a document d by using an Expectation-Maximization (EM) algorithm to estimate both distributions $p(z|d)$ and $p(w|z)$, where z represents a latent topic [33]. Considering that PLSA does not exploit the color name labels of the training images, the PLSA-bg model represents an image d (i.e., document) as a LAB color histogram that contains a group of color bins (i.e., words), and decomposes d into the foreground distribution according to the given color name label l_d (i.e., topic) and the background distribution shared between all training images. By using an EM algorithm to learn the parameters, including the mixing proportion of foreground versus background, the color name distributions, and the background model, the probability of a color name for a given image pixel is represented as [30]:

$$p(z|w) \propto p(z)p(w|z) . \tag{2}$$

where the prior $p(z)$ is uniform over all the color names.

Moreover, besides the probability information of all color names, the proposed CNS model also makes use of the statistical analysis. This is achieved by a color name histogram, in which eleven color bins are involved for measuring color differences. In [9], the HC method directly uses color statistics to define the saliency value for each bin of the color histogram. Compared with HC, our model solely exploits the color name histogram of an input image to compute weighting coefficients and further produce weighted master attention maps. The color name histogram does not participate in the generation of original attention maps, which are still determined by the topological structure of a visual scene.

III. Color Name Space Based Saliency Detection

To incorporate more color information, we extend the BMS model [5] from the LAB color space to the color name space. Two saliency cues, i.e., surroundedness and color, are separately invoked to produce two kinds of saliency maps. They are then fused into one single map for inferring the final result. These steps are described in the following sections.

A. General Framework

As illustrated in Fig. 2, the integrated framework of our saliency model includes two computational pipelines:

Pipeline I. Each input RGB image is first resized to 400 pixels in width and then converted to the color name space. The resultant space is composed of eleven monochrome intensity components, namely color name channels. Following BMS, a set of attention maps is generated based on a Gestalt principle. The attention maps of each channel are linearly fused to produce a master attention map. Finally, the mean attention map $\bar{A}$ is obtained by combining the 11 master attention maps and further post-proccessed to form the saliency map S.

Pipeline II. The resized RGB image is first converted to a *Color Name Image*, from which we can derive two statistical characteristics: 1) a color name histogram which consists of 11 total color levels, and 2) 11 binary indexed matrices where each of them represents the distribution of the corresponding color name. By incorporating two types of weighting patterns, we measure color differences and obtain 11 weighted master attention maps. All the master attention maps generated in Pipeline I also participate in this process. The weighted saliency

map S_w is then obtained through the same combination and post-processing procedure as used in the first pipeline.

Combination. The two saliency maps S and S_w are fed into a truncation procedure to produce the saliency map $\bar{S}$, which simultaneously codes for the topological structure and the color conspicuity over the entire scene. In addition, we apply another post-processing procedure to generate the final result, in which the salient regions are evenly highlighted and smoothed for convenience in the future task of object segmentation.

B. Color Name Channel Based Attention Map

First, we directly use the **im2c** function provided by [30] to generate the color name space $\mathbf{C} = \{C_1, C_2, \ldots, C_{11}\}$ in Pipeline I.[1] In this format, image data consists of 11 color name channels with the range of values $[0, 1]$. Thus, for an input RGB image I, the color representation of each pixel is mapped from the 3-dimensional RGB value to a probabilistic 11-dimensional (11-D) vector which sums up to 1. Considering that the topological structure of I is independent of the perceptual color coherence, each channel is treated equally and normalized to the interval $[0, 255]$ for the subsequent thresholding operation.

Then, we use a set of sequential thresholds from 0 to 255 with a step size of δ to binarize each channel $C_i \in \mathbf{C}$ to n boolean maps:

$$B_i^j = \texttt{THRESH}\,(C_i, \theta_j)\ . \tag{3}$$

where at each threshold θ_j, the above function generates a boolean map B_i^j from C_i by setting all values above θ_j to 1s and replacing all others with 0s. After two morphological operations on B_i^j, including closing and hole-fill, we use a flood-fill algorithm to mask out all the foreground regions connected to the image border to obtain the corresponding attention map A_i^j. The same processing steps are also executed for the complement image $\widetilde{B}_i^j$. As summarized in Algorithm 1, two parameters are required in this stage: the sample step δ, and the kernel radius ω_c of the closing operation. We will discuss the influences of them in Section IV-C.

However, different from BMS where all the attention maps generated from three color channels of the LAB space are linearly fused into one single mean attention map, the proposed CNS model separately computes the average for each color name channel. Suppose that n pairs of attention maps A_i^j and $\widetilde{A}_i^j$ are obtained from C_i, they share the same weight and are averaged into a single new map, which we call "master attention map" in this paper. Then, the mean attention map $\bar{A}$ can be further calculated as the average of 11 master attention maps as follows:

$$A_i = \frac{1}{2n} \sum_{j=1}^{n} \left(A_i^j + \widetilde{A}_i^j \right), \tag{4}$$

$$\bar{A} = \frac{1}{11} \sum_{i=1}^{11} A_i\ . \tag{5}$$

[1]The **im2c** function is available at http://lear.inrialpes.fr/people/vandeweijer/color_names.html, in which the authors also provide a 32,768 lookup table for mapping color values to probabilities over the eleven color names.

Algorithm 1 attention map computation

Input: RGB image I
Output: attention maps A_i^j, $\widetilde{A}_i^j$

convert I from RGB to the color name space $\mathbf{C}$
for each $C_i \in \mathbf{C}$ **do**
  for $\theta_j = 0 : \delta : 255$ **do**
    $B_i^j = \texttt{THRESH}(C_i, \theta_j)$
    $B_i^j = \texttt{CLOSE}(B_i^j, \omega_c)$
    $B_i^j = \texttt{HOLE-FILL}(B_i^j)$
    $A_i^j = \texttt{FLOOD-FILL}(B_i^j)$

    $\widetilde{B}_i^j = \texttt{INVERT}(B_i^j)$
    $\widetilde{B}_i^j = \texttt{CLOSE}(\widetilde{B}_i^j, \omega_c)$
    $\widetilde{B}_i^j = \texttt{HOLE-FILL}(\widetilde{B}_i^j)$
    $\widetilde{A}_i^j = \texttt{FLOOD-FILL}(\widetilde{B}_i^j)$
  end for
end for

Actually, if we merge Eqs. (4) and (5), we can get the same computation procedure of $\bar{A}$ as introduced in the BMS model. The key to the slight difference lies in the 11 master attention maps stored in the intermediate module. In Pipeline I, the computation of $\bar{A}$ is mainly based on the surroundedness cue inferred from the topological structures of the 11 color name channels. For the sake of making better use of the color name space, the proposed framework couples the topological information with two color cues to compute the color based saliency. In Section III-D, we will again employ the 11 master attention maps to produce another mean attention map $\bar{A}_w$.

C. Post-processing

The obtained mean attention map $\bar{A}$ is a double-precision image array. Then we normalize it to have values between 0 and 1, as shown in Fig. 3a. However, due to the existence of other surrounded objects that have clear boundaries and apparently uniform colors (for example, the red flower below the cat), there are several small salient regions in $\bar{A}$. In order to outstand the main salient object (i.e., the cat), we also follow the BMS model to remove these small regions by sequentially performing two steps of morphological reconstruction operations [34], [35] on $\bar{A}$ and its complement image respectively. The structuring element used here is a disk shape with radius ω_r. Figure 3b

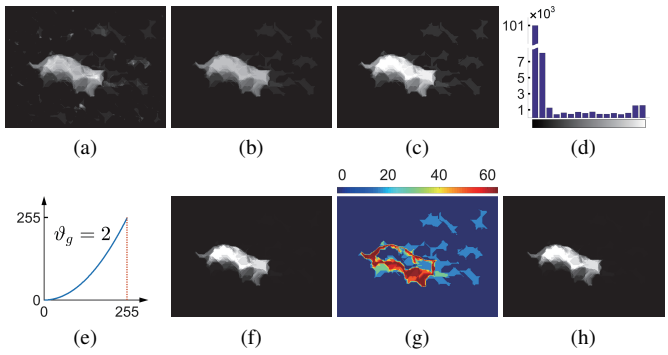

Figure 3. Post-processing. (a) Mean attention map $\bar{A}$. (b) Morphological reconstruction. (c) Normalization result, and (d) its histogram. (e) Intensity mapping curve. (f) Result of enhancing (c) with $\vartheta_r = 0.003$ and $\vartheta_g = 2$. (g) Difference between (c) and (f). (h) Saliency map S.

shows the reconstrution result. It can be observed that those small salient regions have been erased while the original shape of the salient cat is remained.

For a single input image, the ideal output of salient object detection should be a binary map where the pixel values of the salient objects are 1s while others are 0s. However, the disadvantage of the reconstruction procedure is that the high intensity values of the salient pixels are suppressed simultaneously. In addition, the background of the reconstruction result also contains some inconspicuous regions with non-black colors, which would decrease the detection precision. To address the above issues, a nonlinear transformation function is therefore introduced for image enhancement by mapping the intensity values in the reconstruction result to a new range. Overall, we wish to weight the mapping toward lower output values and map all intensity values above a specific threshold to the fixed value 1. Suppose that F is an input map, the intensity transformation function has the syntax form as follows:

$$\mathrm{G} = \textbf{ADJUST}\,(\mathrm{F},\quad [0\quad T_\mathrm{F}/255],\quad [0\quad 1],\quad \vartheta_g)\;, \tag{6}$$

where T_F denotes a truncation threshold in the integer range $[0, 255]$, and ϑ_g determines the mapping relationship between the intensity values in F and G. To suppress non-salient pixels, the lower limit of the mapping is set to 0 and ϑ_g should be set to be greater than 1.

In Eq. (6), all the image intensity values above the truncation threshold T_F (i.e., in the interval $[T_\mathrm{F}, 255]$) are clipped and mapped to 1. For automatically obtaining T_F, we base on the statistical information extracted from the image histogram. After scaling the entire range of values in the reconstruction result to the integer interval $[0, 255]$ (Fig. 3c), we obtain its histogram H with 256 total possible intensity levels (Fig. 3d), where H_i is the number of pixels at the ith gray level. By summing up the number of pixels in H from the gray level 0, the minimum threshold value k is returned and assigned to T_F for ensuring the non-salient pixels cover no less than $(1 - \vartheta_r)$ of the total number of image pixels:

$$T_\mathrm{F} = \arg\min_k \left((1-\vartheta_r) \sum H_i \quad \leq \quad \sum\nolimits_{i=0}^{k} H_i \right)\;. \tag{7}$$

where ϑ_r is empirically set to be less than 10%. For convenience, we merge Eqs. (6) and (7), and abbreviate it as:

$$\mathrm{G} = \textbf{ADJUST}\,(\mathrm{F}, \vartheta_r, \vartheta_g)\;. \tag{8}$$

Figure 3e illustrates the intensity mapping curve with $\vartheta_r = 0.003$ and $\vartheta_g = 2$. Using these parameter settings, we obtain the truncation threshold $T_\mathrm{F} = 255$. This means that the intensity range of the output map (Fig. 3f) is the same as that of the input (Fig. 3c), but the lower (darker) input values are further suppressed. The difference between the two maps is shown in Fig. 3g. Note that on the right side of the cat, those non-salient regions with gray value equal to 16 have been eliminated in the enhancement result.

Finally, we perform a morphological hole-fill operation on the enhancement result to generate the first saliency map S, as shown in Fig. 3h. In an intensity map, a hole is a set of connected dark pixels surrounded by lighter pixels. However, due to the non-existence of dark holes in this case, we obtain the same output map S as Fig. 3f. The effect of the hole-fill operation will be demonstrated in the next subsection. The whole post-processing procedure is summarized in Algorithm 2. Similarly, we will discuss the influences of the three required parameters ω_r, ϑ_r, and ϑ_g in Section IV-C.

Algorithm 2 post-processing

Input: mean attention map $\bar{A}$
Output: saliency map S
1: $S = \textbf{NORMALIZE}(\bar{A}, [0, 1])$
2: $S = \textbf{RECONSTRUCT}(S, \omega_r)$
3: $S = \textbf{NORMALIZE}(S, [0, 255])$
4: $S = \textbf{ADJUST}(S, \vartheta_r, \vartheta_g)$
5: $S = \textbf{HOLE-FILL}(S)$

D. Global Color Cue Based Saliency Map

As indicated previously in Section I, now we introduce a color based saliency algorithm to overcome the limitation of only using topological structural information. In order to take advantage of the 11 color attributes, two global color cues, including probability and contrast, are inferred from a color name image and employed to compute the corresponding weighting coefficients and matrices. The 11 master attention maps obtained in Section III-B are also coupled with these weights to further produce the weighted saliency map S_w.

The input image I is first converted to a color name image M by again using the **im2c** function [30], as shown in Pipeline II of the proposed framework. At each pixel coordinate (x, y), we aim to find the largest element in the probabilistic 11-D color vector, and assign its index to the element $\mathrm{M}(x, y)$ at the same coordinate (x, y) in M. Thereby, different from the probabilistic outputs in Section III-B, the obtained M is an indexed map where each pixel has an integral value from 1 to 11. Basing on the statistics and contrasts of the color names respectively, we obtain two kinds of weights.

1) Color Name Statistic Based Weights: The histogram of M has totally 11 levels in the range $[1, 11]$, where the ith level corresponds to the number of pixels in M having the color name t_i (cf. Table I). If we use the corresponding RGB value c_i to represent each bin, we get a color histogram which is called *Color Name Histogram* in this paper. Subsequently, eleven probability values can be obtained based on the color name statistics of the histogram, where we use f_i to denote the probability of t_i.

Another cue is the distributions of all the color names in the indexed map M. For the purpose of combining with the master attention maps obtained by exploiting the surroundedness cue, we construct 11 indexed matrices using Eq. (9). In each M_i, any element value equal to i is set to 1, and all others are set to 0.

$$M_i(x, y) = \begin{cases} 1\,, & \text{if}\quad \mathrm{M}(x, y) = i \\ 0\,, & \text{otherwise} \end{cases} \tag{9}$$

As discussed in Section III-B, the attention map A_i of the ith color name channel is obtained by linearly summing a set of boolean maps, where all the foreground regions that connected to the image borders are abandoned. For a single boolean map, all the pixels in the remaining surrounded regions share the

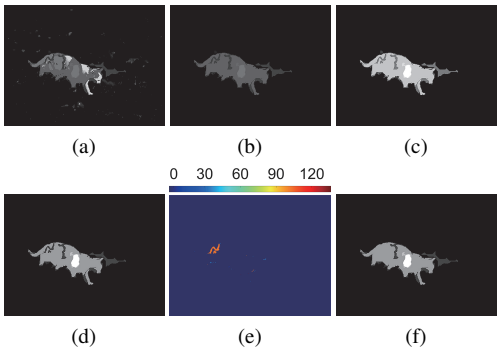

Figure 4. Global color cues based saliency. (a) Weighted mean attention map $\bar{A}_w$. (b) Morphological reconstruction. (c) Normalization. (d) Enhancement result. (e) Filling dark holes in (d). (f) Weighted saliency map S_w.

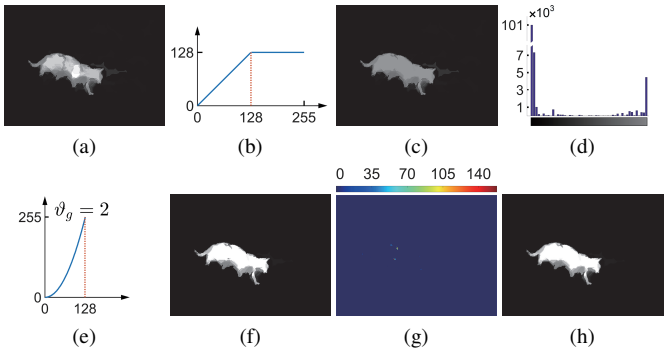

Figure 5. Combination. (a) Original output of averaging Figs. 3h and 4f. (b) Truncation curve. (c) Mean saliency map $\bar{S}$, and (d) its histogram. (e) Intensity mapping curve. (f) Enhancement result. (g) Hole-fill. (h) Final result of CNS.

same weight relevant to the topological information, but occupy different color names. To jointly consider the frequencies and distributions of different color names, we simply combine f_i and M_i to obtain the first kind of weights, i.e., 11 weighting matrices:

$$W_i = f_i M_i \,, \tag{10}$$

2) Color Name Contrast Based Weights: Mainly inspired by [25] and [9], we calculate the second kind of weights, i.e., 11 contrast based weighting coefficients, by also exploiting the color name histogram. In a color name image, the weight of a color name is defined as its color contrast to all other color names, and all pixels with the same color name share the same weight. For the color distance metric, we directly use the corresponding RGB values of the 11 color names given in Table I. Specifically, the weighting coefficient w_i of a color name t_i is defined as:

$$w_i = \begin{cases} \sum_{j=1}^{11} f_j \left\| c_i - c_j \right\|_2^2 \,, & \text{if} \quad f_i \neq 0 \\ 0 \,, & \text{otherwise} \end{cases} \tag{11}$$

where $\left\| c_i - c_j \right\|_2$ is the ℓ_2-norm of the color difference between two color names t_i and t_j.

Overall, the computational procedure of w_i is similar to the HC method [9] except the "otherwise" branch. The color name space in our model is consisted of 11 probabilistic maps, but the color name image is an indexed map. For a pixel with probabilistic 11-D color vector, we ignore those elements with smaller probabilities and assign the element index of the largest probability to the corresponding location in the indexed map. To avoid invoking the irrelevant saliency for those non-existent color names, the coefficient w_i will be set to 0 if t_i does not appear in the color name image. Another noticeable difference compared to HC is the usage of the color name histogram. In this stage, we only compute the weighting values from the histogram, rather than use it to directly define the saliency for each color name.

By integrating the two kinds of weights into the 11 master attention maps $\{A_1, \ldots, A_{11}\}$ and averaging the outputs, we get the weighted mean attention map $\bar{A}_w$ (see Fig. 4a) by:

$$\bar{A}_w = \sum_{i=1}^{11} w_i \cdot \mathbf{N}(W_i \otimes A_i) \,. \tag{12}$$

where $\otimes$ denotes the element-wise matrix product, and $\mathbf{N}(\cdot)$ is a normalization function which sets the values in $\bar{A}_w$ to $[0, 1]$. Figures 4b–4e illustrate the same post-processing procedure introduced in Section III-C. Note that the hole-fill operation completes the closed dark regions inside the salient cat. Finally, we obtain the second saliency map, i.e., the weighted saliency map S_w with the range $[0, 255]$, as shown in Fig. 4f.

E. Combination

To couple with the two saliency maps S and S_w generated using the surroundedness and color cues, we simply average them at the first step of the final stage. The original output is illustrated in Fig. 5a. However, considering that the use of the obtained output is to assist in the task of salient object segmentation, this result is obviously not ideal. For one thing, for the purpose of eliminating the perceptually insignificant regions outside the cat, we perform an intensity adjustment in the post-processing procedure, which simultaneously suppresses the inner saliency and subsequently results in an indeterminate object region in S. For another, in S_w the salient object has a clear contour, but apparently shows a nonuniform intensity distribution due to the color contrast based computational mode. Moreover, the locations of the regions with higher saliency values are completely different between the two maps.

In order to address the above issues, a truncation operation is introduced to clip the original output in this stage. Intuitively, we wish the resultant salient object to have a uniform intensity distribution, which can be further highlighted by a post-processing procedure similar to that used in Section III-C. Since both S and S_w have been normalized to the range $[0, 255]$, we define the improved mean output $\bar{S}$ as:

$$\bar{S} = \frac{[S + S_w]_0^{255}}{2} \,. \tag{13}$$

where $[\,\cdot\,]_0^{255}$ is the operator for truncating the inner to have values between 0 and 255.

As illustrated in Fig. 5b, the above definition causes a piecewise mapping, in which values above 128 are clipped and others stay unchanged. We can see in Fig. 5c that the resultant map $\bar{S}$ occupies the common salient parts between S and S_w. Although the detected object region has lower saliency values,

the whole object is uniform in intensity and clearly stands out of the background. This means that we also can perform a post-processing operation on $\bar{S}$ for refining its saliency values.

Figures 5d–5g illustrate a new post-processing procedure. Compared with Algorithm 2, the difference is that this procedure only includes two operations, i.e., intensity transformation and hole-fill. For the former operation, we use the same parameter settings as before. After filling several small dark holes inside the object region, we obtain the final saliency result of the proposed model, as shown in Fig. 5h. It can be seen that our model well suppresses the unwanted background and uniformly highlights the foreground object. More importantly, for the future task of salient object segmentation, we can easily perform a thresholding operation on the computed saliency map while generate more stable segmentation results over a wide range of thresholds.

IV. Experiments

We evaluate the proposed CNS model with twenty-three saliency models including AC [36], BMS [5], CA [22], COV [6], FES [37], FT [8], GC [38], GMR [11], GR [12], GU [38], HC [9], HFT [7], HS [10], MSS [39], PCA [40], RC [9], RPC [24], SEG [41], SIM [4], SR [3], SUN [42], SWD [43], and SeR [44] on three benchmark datasets: ASD [8], [45], ECSSD [10], [46], and ImgSal [7], [47]. The used saliency maps of the above models are from:

- For the saliency models BMS,[2] HFT,[3] HS,[4] and RPC[5] over all the three evaluation datasets, we use the author-provided saliency results, or run the authors' codes to obtain the saliency maps.
- For the AC, CA, FT, HC, RC, and SR models on the ASD dataset, we directly use the saliency maps provided by Cheng et al. [9].[6] For the remainder models on ASD, we retrieve the related saliency maps from the MSRA10K database [48].[7]
- For the remainder saliency models, we employ the implementation of the salient object detection benchmark published by Borji et al. [49]:[8] on the ECSSD dataset, the saliency maps come directly from the author-provided saliency results; on the ImgSal dataset, we run the authors' source code to generate the saliency maps.

The developed MATLAB code of CNS will be published in our project page: http://www.loujing.com/cns-sod/.

A. Datasets

The popular ASD dataset (a.k.a, MSRA1000) is a subset of MSRA5000 [45].[9] The original MSRA5000 salient object dataset contains 5000 images with the labeled rectangles from nine participants. Achanta et al. [8] consider the use of saliency maps in salient object segmentation, then derive the ASD dataset with 1000 images from MSRA5000. Instead of the user-drawn rectangles around salient regions used in [45], the ASD dataset provides the object-contour based ground truth for more accurate comparisons of segmentation results.[10]

The ECSSD dataset is an extension of CSSD.[11] In order to represent more general situations of natural images than ASD, Yan et al. construct the CSSD dataset, which contains 200 images with diversified patterns in both foreground and background [10]. Subsequently, the authors extend CSSD to a larger dataset named ECSSD, which includes 1000 structurally complex images and the pixel-wise ground truth masks labeled by five helpers [46].

In addition, we evaluate the proposed model on the ImgSal dataset, which is designed for the detection of salient regions of different size [7], [47].[3] This dataset contains 235 images collected using Google, and provides both human labeled region ground truth and eye fixation ground truth. For the region ground truth, the authors ask nineteen naive subjects to label the images in a random manner, and generate two kinds of labeling results for each input image: binary map and probability map. In our experiments, we only use the binary masks for evaluating saliency detection results.

B. Experimental Setup

The common used metrics to evaluate salient object detection models are *Precision-Recall* and *F-measure*. For an input image, the resultant saliency map $\bar{S}$ is a gray-scale image having integer values in the range $[0, 255]$. So we can partition $\bar{S}$ to a binary mask M with a threshold ($\in [0, 255]$), and compute precision and recall by comparing M with the corresponding ground truth G as follows:

$$Precision = \frac{|M \cap G|}{|M|}, \quad Recall = \frac{|M \cap G|}{|G|}, \tag{14}$$

where $|\cdot|$ indicates the number of the foreground pixels in a binary map. Moreover, to jointly evaluate precision and recall, the F-measure value can be obtained by:

$$F_\beta = \frac{(1 + \beta^2) \times Precision \times Recall}{\beta^2 \times Precision + Recall}. \tag{15}$$

where β^2 is set to 0.3 for emphasizing the precision score as suggested in [8].

In our experiments, two binarization ways are introduced to partition all the resultant saliency maps.

1) Fixed Thresholding: For the whole dataset, we vary the threshold T_f from 0 to 255 to get the average scores of precision, recall and F-measure (i.e., F_β) at each value of T_f. Besides plotting the precision-recall and F-measure curves, we compute two F_β statistics of each saliency model for quantitative evaluation, i.e., the average F_β score (denoted "AvgF") and the maximum F_β score (denoted "MaxF").

[2]The code is available at http://cs-people.bu.edu/jmzhang/BMS/BMS.html.

[3]The code comes from the ImgSal saliency database: http://www.escience.cn/people/jianli/DataBase.html, in which the image set and region ground truth are both provided.

[4]The executable can be downloaded from http://www.cse.cuhk.edu.hk/leojia/projects/hsaliency/.

[5]The saliency maps are available at http://www.loujing.com/rpc-saliency/.

[6]The saliency detection results of these models can be downloaded from http://cg.cs.tsinghua.edu.cn/people/~cmm/Saliency/Index.htm.

[7]The database is available at http://mmcheng.net/msra10k/.

[8]The online benchmark website: http://mmcheng.net/salobjbenchmark/.

[9]The image set of MSRA5000 can be downloaded from http://research.microsoft.com/en-us/um/people/jiansun/SalientObject/salient_object.htm.

[10]The ground truth database is available at http://ivrl.epfl.ch/supplementary_material/RK_CVPR09/.

[11]The images and ground truth masks of CSSD and ECSSD can be downloaded from http://www.cse.cuhk.edu.hk/leojia/projects/hsaliency/dataset.html.

2) Adaptive Thresholding: As presented in [8], we use an adaptive threshold T_a (cf. Eq. (16)) to partition each saliency map and compute the average scores of precision, recall and F_β over the whole dataset. Besides plotting the precision-recall bars, we also report the F_β score obtained using the adaptive threshold (denoted "AdaptF") of each saliency model.

$$T_a = \frac{2}{W \times H} \sum_{x=1}^{W} \sum_{y=1}^{H} \bar{S}(x, y)\,. \tag{16}$$

where W and H are the width and height of $\bar{S}$ respectively, $\bar{S}(x, y)$ is the saliency value of $\bar{S}$ at the coordinate (x, y).

C. Parameter Analysis

The proposed model includes five parameters: sample step δ, kernel radius ω_c of closing operation, kernel radius ω_r of morphological reconstruction, saturation ratio ϑ_r, and gamma ϑ_g of intensity mapping curve. To find the optimal parameter values for each dataset, as suggested in [50], we exploit the "MaxF" metric to compare the quality of the saliency maps obtained using different parameter settings. After 256 F_β scores have been computed by fixed thresholding, the maximum one of them is selected as the best score for each group of parameter setting. In the experimental implementation, the ranges of the five parameters are: $\delta \in [4 : 4 : 40]$, $\omega_c \in [1 : 1 : 20]$, $\omega_r \in [1 : 1 : 20]$, $\vartheta_r \in [0.001 : 0.001 : 0.009] \cup [0.01 : 0.01 : 0.1]$, and $\vartheta_g \in [1.0 : 0.1 : 3.0]$.

Figure 6 shows the influences of the five parameters on all three benchmark datasets. First, the proposed CNS model is not sensitive to the parameter ϑ_g, while varying ϑ_g from 1.0 to 3.0 rarely changes the MaxF scores over each dataset. Second, the parameters ω_c, ω_r, and ϑ_r have direct impacts on the MaxF scores especially on the ImgSal dataset. Overall, each MaxF curve shows a slight upward trend as the parameter value increases, and then starts to drop after the MaxF reached the summit. Compared to the first two datasets, the influences of the above three parameters are more apparent on ImgSal. Third, the sample step δ does not significantly impact on the saliency detection results produced by our model on ASD and ECSSD, and all the resultant MaxF curves do not clearly show the unimodal distributions especially on ImgSal. However, the runtime of our model is directly influenced by the sample step. As can be easily found, as the value of the parameter δ decreases, it typically leads to more boolean maps and correspondingly lower performance on test images.

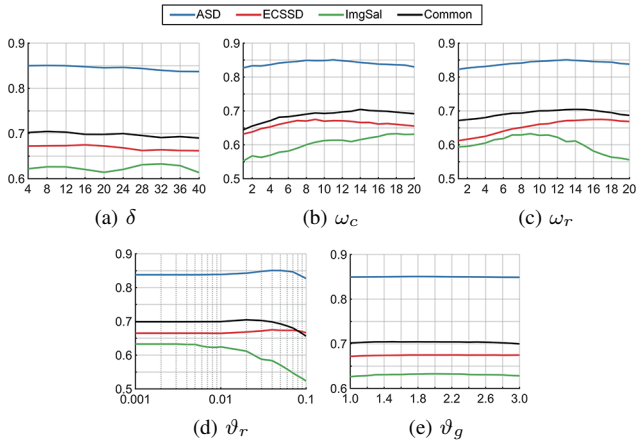

Figure 6. Parameter analysis of CNS.

Table II
OPTIMAL AND COMMON PARAMETER VALUES

Dataset	δ	ω_c	ω_r	ϑ_r	ϑ_g
ASD [8], [45]	8	11	13	0.04	1.8
ECSSD [10], [46]	16	9	17	0.04	2.2
ImgSal [7], [47]	32	18	9	0.003	2
Common	8	14	14	0.02	1.5

We report the optimal parameter settings of different datasets in Table II. Except ASD, ECSSD, and ImgSal, we further aim to find a common parameter setting for other saliency datasets. Based on the diversity of the three datasets used in our experiments, here we introduce the average MaxF metric for parameter selection. After three MaxF curves have been obtained for each parameter, we simply average three MaxF scores at each parameter value, then choose the location of the maximum as the optimal value for this parameter. Figure 6 also shows the influence of the common parameter setting, in which the black curves, indicated by "Common", exhibit the trends of five parameters in their ranges of values. Over all the datasets and parameters, the performances are better on ASD, resulting in the similar trends compared with the curves using the common parameter setting. In Table II, we also report the common parameter values, it can be noticed that they are more close to the optimal parameter values of the ASD dataset.

D. Results

We present the statistical comparison results of the proposed CNS model compared with twenty-three saliency detection models on the three benchmark datasets. For each dataset, the results obtained by using two versions of the parameter setting are both reported, i.e., the optimal and common parameters. We use the shorthands CNSo and CNSc to distinguish them in the experiments, where the lowercase letters *o* and *c* are the abbreviations of *optimal* and *common*, respectively. Figures 7a and 7b show the precision-recall and F-measure (i.e., F_β) curves produced by fixed thresholding. The precision-recall bars generated by utilizing the adaptive threshold T_a are presented in Fig. 7c. More quantitative details are given in Fig. 9.

Due to the intensity mapping in the post-processing procedure, the resultant curves of our model clearly present two noticeable characteristics: one is that the recall scores span a more narrow range of the output domain; the other is that each F-measure curve tends to be more flat after it rapidly reaches the summit. Although having some disadvantages in the precision, our model has higher F_β scores than the other saliency models at most thresholds, especially on the ECSSD and ImgSal datasets. The crucial advantage of our model indeed is associated with the essential task of salient object detection, which is to solve a salient foreground segmentation problem [49].

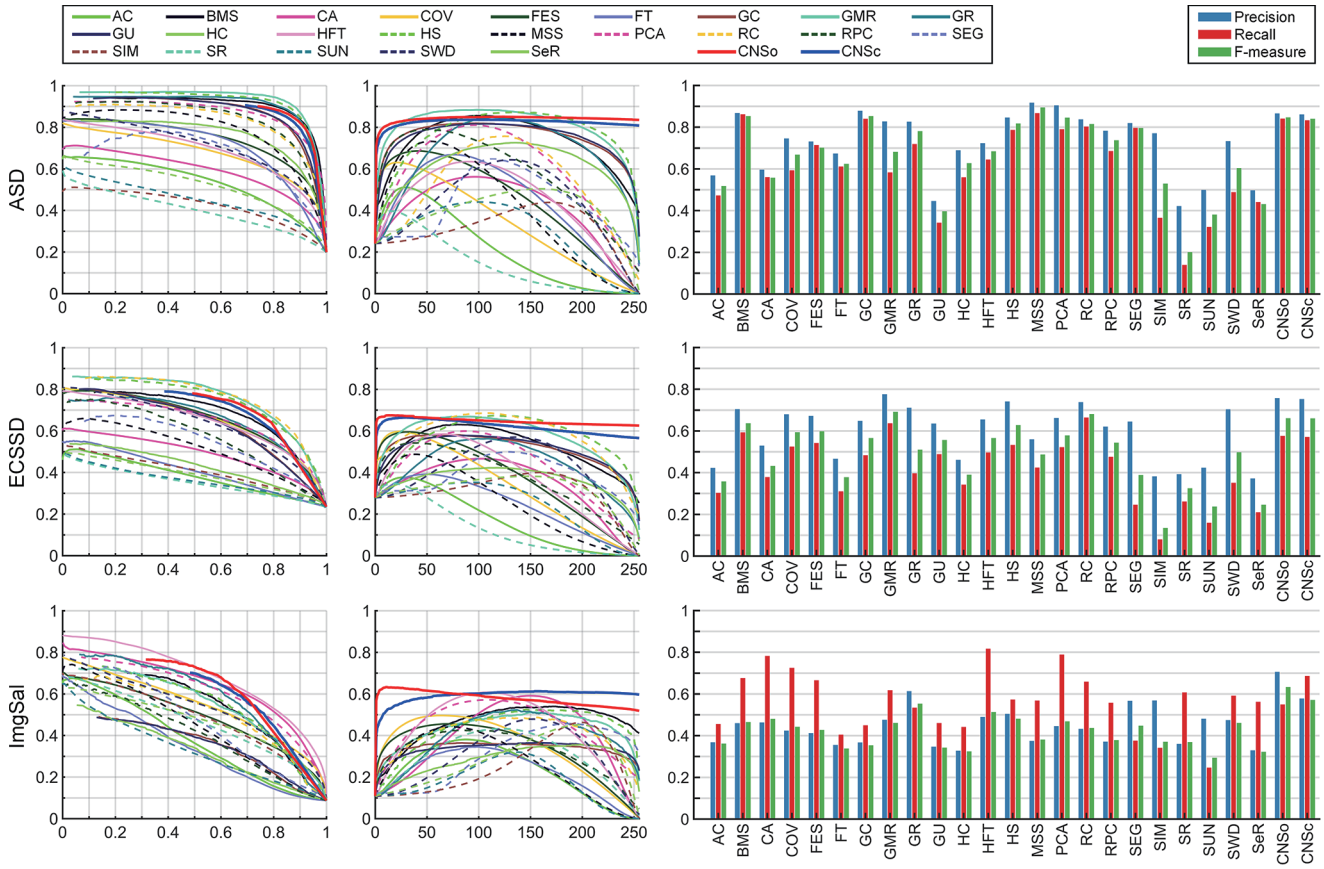

Figure 7. Performance of the proposed CNS model compared with twenty-three saliency models on the ASD (top), ECSSD (middle), and ImgSal (bottom) datasets, respectively. (a) Precision (y-axis) and recall (x-axis) curves. (b) F-measure (y-axis) curves, where the x-axis denotes the threshold T_f in the integer range $[0, 255]$. (c) Precision-recall bars.

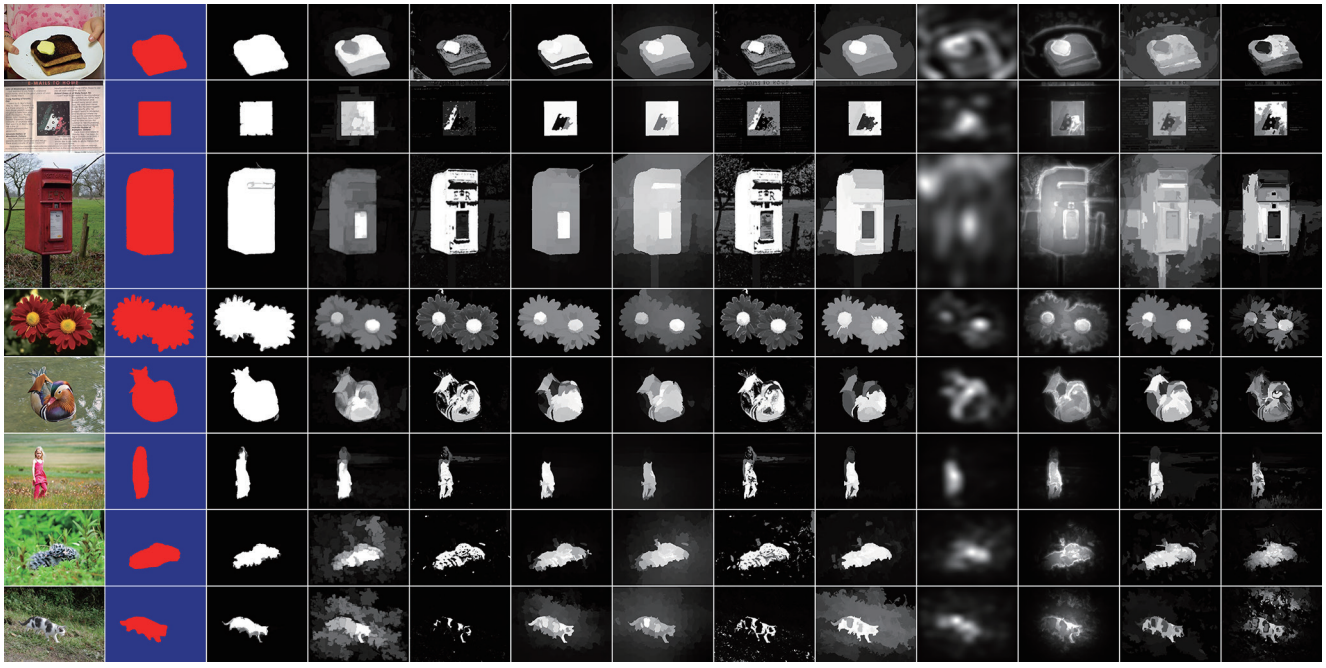

(a) Input (b) GT (c) CNS (d) BMS [5] (e) GC [38] (f) GMR [11] (g) GR [12] (h) GU [38] (i) HS [10] (j) HFT [7] (k) PCA [40] (l) RC [9] (m) RPC [24]

Figure 8. Visual comparison of salient object detection results. Top three rows, middle two rows, and bottom three rows are images from the ASD, ECSSD, and ImgSal datasets, respectively. (a) Input images, and (b) their ground truth masks. Saliency maps produced using (c) the proposed CNS model, and (d)–(m) other ten saliency models.

Model (F_β)	ASD [8], [45]			ECSSD [10], [46]			ImgSal [7], [47]			Average		
	AvgF	MaxF	AdaptF	AvgF	MaxF	AdaptF	AvgF	MaxF	AdaptF	AvgF	MaxF	AdaptF
AC [36]	.2139	.5107	.5174	.1688	.3766	.3575	.2298	.3807	.3611	.2042	.4227	.4120
BMS [5]	.7296	.8558	.8528	.5193	.6303	.6363	.4608	.5399	.4644	.5699	.6753	.6512
CA [22]	.4043	.5615	.5569	.3403	.4661	.4314	.3913	.5910	.4801	.3786	.5395	.4895
COV [6]	.3413	.6305	.6264	.3347	.5973	.5931	.3485	.4960	.4419	.3415	.5746	.5538
FES [37]	.4484	.6859	.6840	.3762	.5951	.5976	.3371	.4557	.4268	.3872	.5789	.5695
FT [8]	.4342	.6681	.6677	.2419	.3915	.3775	.2234	.3451	.3380	.2998	.4682	.4611
GC [38]	.7474	.8193	.8169	.5118	.5814	.5652	.3381	.3642	.3531	.5324	.5883	.5784
GMR [11]	.8034	.8838	.8941	.5697	.6687	.6909	.4345	.5119	.4607	.6025	.6881	.6819
GR [12]	.6730	.8479	.8451	.4326	.5631	.5095	.3930	.5236	.5532	.4995	.6449	.6359
GU [38]	.7454	.8164	.8141	.5103	.5774	.5558	.3339	.3646	.3419	.5299	.5862	.5706
HC [9]	.6113	.7255	.7009	.3642	.4224	.3894	.2849	.3561	.3238	.4202	.5013	.4714
HFT [7]	.4412	.6347	.6231	.3739	.5849	.5653	.4254	.6079	.5129	.4135	.6091	.5671
HS [10]	.7628	.8722	.8527	.5674	.6732	.6273	.4365	.5248	.4803	.5889	.6901	.6534
MSS [39]	.4116	.7321	.7369	.2543	.4873	.4864	.2656	.4415	.3807	.3105	.5536	.5347
PCA [40]	.5884	.8101	.7953	.4252	.5987	.5778	.4415	.5718	.4679	.4850	.6602	.6137
RC [9]	.5192	.7570	.6809	.5766	.6860	.6801	.4048	.4871	.4365	.5002	.6434	.5992
RPC [24]	.5798	.7886	.7800	.3745	.5424	.5431	.3270	.4245	.3783	.4271	.5852	.5671
SEG [41]	.4305	.6485	.5288	.3840	.4990	.3883	.3096	.4569	.4470	.3747	.5348	.4547
SIM [4]	.3162	.4384	.2002	.3080	.3998	.1342	.2497	.4626	.3698	.2913	.4336	.2347
SR [3]	.1435	.3964	.3964	.1275	.3469	.3246	.3006	.4324	.3687	.1905	.3919	.3632
SUN [42]	.2916	.4402	.3803	.2442	.3522	.2365	.1764	.3198	.2937	.2374	.3708	.3035
SWD [43]	.4399	.6434	.6033	.4074	.5700	.4971	.3016	.4787	.4605	.3830	.5640	.5203
SeR [44]	.3975	.5037	.4300	.3179	.3818	.2452	.2855	.4513	.3216	.3336	.4456	.3323
CNSo	.8380	.8505	.8468	.6451	.6748	.6600	.5767	.6326	.6326	.6866	.7193	.7131
CNSc	.8204	.8361	.8398	.6191	.6645	.6593	.5902	.6127	.5702	.6765	.7044	.6898
Average	.5253	.6943	.6668	.3998	.5332	.4932	.3547	.4733	.4266	.4266	.5670	.5289

Figure 9. Statistics of average F_β (AvgF), maximum F_β (MaxF), and F_β using adaptive threshold (AdaptF) on the three benchmark datasets. The top three scores under each evaluation metric are highlighted in red, green, and blue, respectively. See the text for details.

A good salient object detection model should generate accurate saliency maps with evenly highlighted foreground and thoroughly suppressed background. One obvious way to extract salient objects from the background is to binarize the saliency map with a fixed threshold, which might be quite difficult to automatically determine. In practice, we usually exploit the maximum F_β score (i.e., MaxF) of the F-measure curve to evaluate the performance of a saliency model, and choose the location of the MaxF as the optimal segmentation threshold [50]. Obviously, for a test dataset, suppose that each resultant saliency map is the same as the corresponding ground truth mask, then the F-measure curve would be a horizontal line. Contrarily, if the resultant F-measure curve produced by a saliency model is a horizontal line, we can obtain the identical segmentation result at any threshold from 0 to 255. Therefore, for two models with the same MaxF, we prefer to select the model which results in a more flat F-measure curve. This means that the segmentation results using this model would be more stable (that is, virtually unchanged) over a wide range of thresholds.

Figure 8 shows a visual comparison of the saliency maps obtained by different models. Note that the results of our model are produced using the optimal parameter values of each evaluated dataset (see Table II).[12] For each example image, we see that the proposed model generates more accurate saliency map, which is very close to the corresponding ground truth mask. Each resultant salient region detected by our model has high and uniform intensity, and well-defined boundary, resulting in a simple thresholding for salient object segmentation.

In Fig. 9, we report the quantitative statistics of the three evaluation metrics discussed earlier. The baseline scores, indicated by "Average", are simply the average of evaluation scores of all saliency models on the test datasets. With respect to the AvgF score, the proposed model outperforms all other models on all datasets. Obviously, this is mainly owed to more flat F-measure curves in a wide range of thresholds. Besides, the three best models are GMR, RC, and BMS.

However, on the ASD and ECSSD datasets, our model has no advantages in terms of both MaxF and AdaptF scores. With respect to the AdaptF, GMR performs the best on these two datasets; it also ranks the first on the ASD dataset using the MaxF measure. By using the two different parameter settings, our model ranks the fourth (CNSo) and the sixth (CNSc) on ASD; while on ECSSD, CNSo is still among top three models in terms of both MaxF and AdaptF scores, but CNSc ranks the fifth and the fourth using the MaxF and AdaptF metrics respectively. However, on the ImgSal dataset, our model again outperforms all other models with large margins. Other top three contenders on ImgSal are HFT, GR and BMS. The GMR

[12]See our project page for all the saliency maps of CNSo and CNSc.

model is not on the list of top five models using any evaluation metric. Moreover, compared to the ASD and ECSSD datasets, the average performances of all models are lower on ImgSal, implying that this dataset is more challenging because the images collected in it contain salient regions of different sizes.

Finally, on average, the proposed model performs the best over all saliency models and evaluation metrics. Besides, the two best models are HS and GMR. The MaxF scores of eleven models are lower than the average score. The top five worst models are SeR, SIM, AC, SR, and SUN. Except AC, all the other four models are eye fixation prediction models, which have no advantage for salient object detection because the output saliency maps of them are blurred and sparse. But this dose not necessarily mean that eye fixation prediction models are not suitable for detecting salient objects. For example, the BMS model is initially designed for the task of eye fixation prediction. We can see that on average it always ranks the fifth using any metric and performs better than most of the salient object detection models evaluated in our experiments.

E. Discussions

Although CNS performs well on the benchmark datasets, it does fail in some cases. These failures are mainly caused by three visual attributes implicitly used in identifying salient objects: location, color, and size. Figure 10 shows several of the hard image cases collected from the three evaluation datasets. The third row are the color name images annotated by using the corresponding RGB colors in Table I.

- *Location:* The key idea of BMS is the Gestalt principle based surroundedness, thus the regions connected to the image borders are masked out in the generation of attention maps, as shown in Fig. 10b.
- *Color:* The proposed CNS model originates from BMS, and exploits the eleven color channels for figure-ground segregation. Sometimes, the foreground objects do not directly touch the border of an image, but they may have very similar colors to some background elements in the color name image. For example, in the color name images of Figs. 10c and 10d, the RGB colors of the manually labeled salient objects (the horse and the statue) and some background regions (e.g., the valley and the plinth) are almost the same. While the salient objects and the image borders are connected by the background regions, the salient objects are always removed in the generation procedure of attention maps. Moreover, the color statistics based global contrast is also introduced in CNS. The color similarities between the foreground objects and the background elements impact the ability of the proposed model to permit salient objects to literally pop out (cf. Figs. 10a, 10c, and 10d).
- *Size:* In Algorithms 1 and 2, some morphological operations including closing and reconstruction are used to perform saliency map computation. The influences of the parameters ω_c and ω_r have already been presented in Fig. 6. These parameters have a substantial impact on the output of CNS, especially on the ImgSal dataset. As Figs. 10e and 10f show, the manually labeled small salient objects are eroded because the structuring elements chosen in the algorithms are larger than the sizes of these objects.
- Another hard case is caused by the thin artificial black border around some test images, as illustrated in the first row of Fig. 10a. When doing the flood-fill operation on certain boolean maps, CNS regards the inner area as a whole region which is surrounded by an enclosed boundary, and does not set any of the foreground pixels to 0. Such a processing mechanism leaves unchanged background elements inside the black border, and results in the failure of figure-ground segregation.

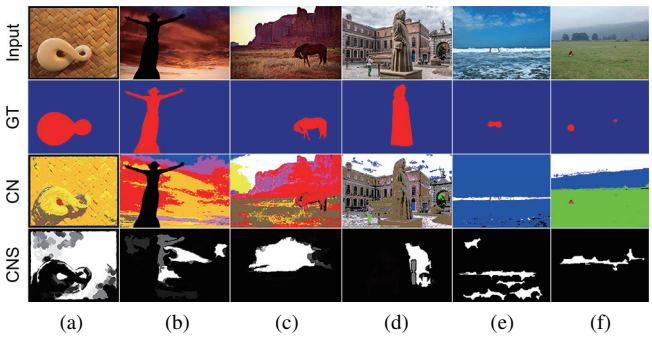

Figure 10. Hard image cases of CNS in detecting salient objects. Left two columns, middle two columns, and right two columns are images from the ASD, ECSSD, and ImgSal datasets, respectively. Input: input images. GT: ground truth masks. CN: color name images. CNS: saliency detection results of the proposed model.

Clearly, the proposed model focuses on bottom-up image processing techniques, and only employs low-level features including color and intensity in its paradigm. Therefore, it fails to highlight the regions that have similar colors to their surroundings. One way to tackle this issue is to invoke more complex visual features. Second, under the definition of surroundedness, the region connected to the image border is not enclosed by a complete outer contour, resulting in the absence of object level information in the attention map computation. Background priors and top-down cues should be employed to solve this problem. Finally, the CNS model works well for detecting large salient objects, but is not suitable for small salient objects. It would be interesting to adopt a multi-scale strategy or automatically seek the optimal scale for the detection of different sizes of salient objects.

V. Conclusions

Throughout this paper, we present a salient object detection model based on the color name space. Considering the outstanding contribution of color contrast for saliency detection, a unified framework is constructed to overcome the limitation of the boolean map based saliency method. By exploring the visual features with respect to linguistic color names, we suggest that the model of fusing color attributes provides superior performance over that only based on topological structure information. Moreover, we propose an improved post-processing procedure to uniformly smooth and highlight the computed salient objects, so that the object regions have high and constant intensity levels for the convenience of future object segmentation. Experimental results indicate the performance improvement of the proposed model on the test datasets.

With regard to future work, first, we intend to invoke a background measure to handle the salient objects that heavily connected to the image borders. Second, it would be interesting to incorporate more visual cues and top-down information to solve the problem of color confusion between the figure and the ground. Third, for each morphological structuring element used in the proposed algorithms, only one fixed value is selected as the optimal kernel radius, resulting in the loss of small salient objects. However, we have noted that an adaptive radius can effectively address this issue. How to automatically determine the radius size is left to future investigation. Finally, the current version of the MATLAB code is implemented for the purpose of academic research. We further plan to optimize our code for improving the speed performance of the proposed model.

ACKNOWLEDGMENTS

The work of J. Lou, L. Chen, W. Zhu, and M. Ren was supported by the National Natural Science Foundation of China under Grant 61231014. H. Wang was supported in part through the National Defense Pre-research Foundation of China under Grant 9140A01060115BQ02002. Q. Xia was supported by the National Natural Science Foundation of China under Grant 61403202, and the China Postdoctoral Science Foundation (No. 2014M561654). The authors thank Andong Wang, Fenglei Xu, and Haiyang Zhang for helpful discussions regarding this manuscript.

REFERENCES

[1] C. Koch and S. Ullman, "Shifts in selective visual attention: Towards the underlying neural circuitry," *Hum. Neurobiol.*, vol. 4, pp. 219–227, 1985.

[2] L. Itti, C. Koch, and E. Niebur, "A model of saliency-based visual attention for rapid scene analysis," *IEEE Trans. Pattern Anal. Mach. Intell.*, vol. 20, no. 11, pp. 1254–1259, 1998.

[3] X. Hou and L. Zhang, "Saliency detection: A spectral residual approach," in *Proc. IEEE Conf. Comput. Vis. Pattern Recognit.*, 2007, pp. 1–8.

[4] N. Murray, M. Vanrell, X. Otazu, and C. A. Parraga, "Saliency estimation using a non-parametric low-level vision model," in *Proc. IEEE Conf. Comput. Vis. Pattern Recognit.*, 2011, pp. 433–440.

[5] J. Zhang and S. Sclaroff, "Saliency detection: A boolean map approach," in *Proc. IEEE Int. Conf. Comput. Vis.*, 2013, pp. 153–160.

[6] E. Erdem and A. Erdem, "Visual saliency estimation by nonlinearly integrating features using region covariances," *J. Vis.*, vol. 13, no. 4, pp. 11: 1–20, 2013.

[7] J. Li, M. D. Levine, X. An, X. Xu, and H. He, "Visual saliency based on scale-space analysis in the frequency domain," *IEEE Trans. Pattern Anal. Mach. Intell.*, vol. 35, no. 4, pp. 996–1010, 2013.

[8] R. Achanta, S. Hemami, F. Estrada, and S. Süsstrunk, "Frequency-tuned salient region detection," in *Proc. IEEE Conf. Comput. Vis. Pattern Recognit.*, 2009, pp. 1597–1604.

[9] M.-M. Cheng, G.-X. Zhang, N. J. Mitra, X. Huang, and S.-M. Hu, "Global contrast based salient region detection," in *Proc. IEEE Conf. Comput. Vis. Pattern Recognit.*, 2011, pp. 409–416.

[10] Q. Yan, L. Xu, J. Shi, and J. Jia, "Hierarchical saliency detection," in *Proc. IEEE Conf. Comput. Vis. Pattern Recognit.*, 2013, pp. 1155–1162.

[11] C. Yang, L. Zhang, H. Lu, X. Ruan, and M.-H. Yang, "Saliency detection via graph-based manifold ranking," in *Proc. IEEE Conf. Comput. Vis. Pattern Recognit.*, 2013, pp. 3166–3173.

[12] C. Yang, L. Zhang, and H. Lu, "Graph-regularized saliency detection with convex-hull-based center prior," *IEEE Signal Process. Lett.*, vol. 20, no. 7, pp. 637–640, 2013.

[13] C. Qin, G. Zhang, Y. Zhou, W. Tao, and Z. Cao, "Integration of the saliency-based seed extraction and random walks for image segmentation," *Neurocomputing*, vol. 129, pp. 378–391, 2014.

[14] J. Lou, W. Zhu, H. Wang, and M. Ren, "Small target detection combining regional stability and saliency in a color image," *Multimed. Tools Appl.*, pp. 1–18, 2016.

[15] Z. Ren, S. Gao, L.-t. Chia, and I. W.-h. Tsang, "Region-based saliency detection and its application in object recognition," *IEEE Trans. Circuits Syst. Video Technol.*, vol. 24, no. 5, pp. 769–779, 2014.

[16] A. Borji, S. Frintrop, D. N. Sihite, and L. Itti, "Adaptive object tracking by learning background context," in *Proc. IEEE Conf. Comput. Vis. Pattern Recognit.*, 2012, pp. 23–30.

[17] C. Guo and L. Zhang, "A novel multiresolution spatiotemporal saliency detection model and its applications in image and video compression," *IEEE Trans. Image Process.*, vol. 19, no. 1, pp. 185–198, 2010.

[18] Y. J. Lee, J. Ghosh, and K. Grauman, "Discovering important people and objects for egocentric video summarization," in *Proc. IEEE Conf. Comput. Vis. Pattern Recognit.*, 2012, pp. 1346–1353.

[19] E. Niebur and C. Koch, "Computational architectures for attention," in *The Attentive Brain*. Cambridge, MA: MIT Press, 1998, ch. 9, pp. 163–186.

[20] A. M. Treisman and G. Gelade, "A feature-integration theory of attention," *Cogn. Psychol.*, vol. 12, no. 1, pp. 97–136, 1980.

[21] Y.-F. Ma and H.-J. Zhang, "Contrast-based image attention analysis by using fuzzy growing," in *Proc. ACM Int. Conf. Multimed.*, 2003, pp. 374–381.

[22] S. Goferman, L. Zelnik-Manor, and A. Tal, "Context-aware saliency detection," in *Proc. IEEE Conf. Comput. Vis. Pattern Recognit.*, 2010, pp. 2376–2383.

[23] D. A. Klein and S. Frintrop, "Center-surround divergence of feature statistics for salient object detection," in *Proc. IEEE Int. Conf. Comput. Vis.*, 2011, pp. 2214–2219.

[24] J. Lou, M. Ren, and H. Wang, "Regional principal color based saliency detection," *PLoS One*, vol. 9, no. 11, pp. e112 475: 1–13, 2014.

[25] Y. Zhai and M. Shah, "Visual attention detection in video sequences using spatiotemporal cues," in *Proc. ACM Int. Conf. Multimed.*, 2006, pp. 815–824.

[26] C. Scharfenberger, A. Wong, and D. A. Clausi, "Structure-guided statistical textural distinctiveness for salient region detection in natural images," *IEEE Trans. Image Process.*, vol. 24, no. 1, pp. 457–470, 2015.

[27] E. Rubin, "Figure and ground," in *Readings in Perception*, 1958, pp. 194–203.

[28] V. Mazza, M. Turatto, and C. Umiltà, "Foreground-background segmentation and attention: A change blindness study," *Psychol. Res.*, vol. 69, no. 3, pp. 201–210, 2005.

[29] S. E. Palmer, *Vision Science: From Photons to Phenomenology*. Cambridge, MA: MIT Press, 1999.

[30] J. van de Weijer, C. Schmid, and J. Verbeek, "Learning color names from real-world images," in *Proc. IEEE Conf. Comput. Vis. Pattern Recognit.*, 2007, pp. 1–8.

[31] J. van de Weijer, C. Schmid, J. Verbeek, and D. Larlus, "Learning color names for real-world applications," *IEEE Trans. Image Process.*, vol. 18, no. 7, pp. 1512–1523, 2009.

[32] B. Berlin and P. Kay, *Basic Color Terms: Their Universality and Evolution*. Berkeley, CA: University of California Press, 1969.

[33] T. Hofmann, "Probabilistic latent semantic indexing," in *Proc. ACM SIGIR Conf. Res. Dev. Inf. Retr.*, 1999, pp. 50–57.

[34] L. Vincent, "Morphological grayscale reconstruction in image analysis: Applications and efficient algorithms," *IEEE Trans. Image Process.*, vol. 2, no. 2, pp. 176–201, 1993.

[35] R. C. Gonzalez, R. E. Woods, and S. L. Eddins, "Morphological image processing," in *Digit. Image Process. Using MATLAB*, 1st ed. Pearson Prentice Hall, 2004, ch. 9, pp. 362–365.

[36] R. Achanta, F. Estrada, P. Wils, and S. Süsstrunk, "Salient region detection and segmentation," in *Proc. Int. Conf. Comput. Vis. Syst.*, 2008, pp. 66–75.

[37] H. R. Tavakoli, E. Rahtu, and J. Heikkilä, "Fast and efficient saliency detection using sparse sampling and kernel density estimation," in *Proc. Scand. Conf. Image Anal.*, 2011, pp. 666–675.

[38] M.-M. Cheng, J. Warrell, W.-Y. Lin, S. Zheng, V. Vineet, and N. Crook, "Efficient salient region detection with soft image abstraction," in *Proc. IEEE Int. Conf. Comput. Vis.*, 2013, pp. 1529–1536.

[39] R. Achanta and S. Süsstrunk, "Saliency detection using maximum symmetric surround," in *Proc. IEEE Int. Conf. Image Process.*, 2010, pp. 2653–2656.

[40] R. Margolin, A. Tal, and L. Zelnik-Manor, "What makes a patch distinct?" in *Proc. IEEE Conf. Comput. Vis. Pattern Recognit.*, 2013, pp. 1139–1146.

[41] E. Rahtu, J. Kannala, M. Salo, and J. Heikkilä, "Segmenting salient objects from images and videos," in *Proc. Eur. Conf. Comput. Vis.*, 2010, pp. 366–379.

[42] L. Zhang, M. H. Tong, T. K. Marks, H. Shan, and G. W. Cottrell, "SUN: A Bayesian framework for saliency using natural statistics," *J. Vis.*, vol. 8, no. 7, pp. 32: 1–20, 2008.

[43] L. Duan, C. Wu, J. Miao, L. Qing, and Y. Fu, "Visual saliency detection by spatially weighted dissimilarity," in *Proc. IEEE Conf. Comput. Vis. Pattern Recognit.*, 2011, pp. 473–480.
[44] H. J. Seo and P. Milanfar, "Static and space-time visual saliency detection by self-resemblance," *J. Vis.*, vol. 9, no. 12, pp. 15: 1–27, 2009.
[45] T. Liu, J. Sun, N.-N. Zheng, X. Tang, and H.-Y. Shum, "Learning to detect a salient object," in *Proc. IEEE Conf. Comput. Vis. Pattern Recognit.*, 2007, pp. 1–8.
[46] J. Shi, Q. Yan, L. Xu, and J. Jia, "Hierarchical image saliency detection on extended CSSD," *IEEE Trans. Pattern Anal. Mach. Intell.*, vol. 38, no. 4, pp. 717–729, 2016.
[47] J. Li, M. D. Levine, X. An, and H. He, "Saliency detection based on frequency and spatial domain analysis," in *Proc. Br. Mach. Vis. Conf.*, 2011, pp. 86: 1–11.
[48] M.-M. Cheng, N. J. Mitra, X. Huang, P. H. S. Torr, and S.-M. Hu, "Global contrast based salient region detection," *IEEE Trans. Pattern Anal. Mach. Intell.*, vol. 37, no. 3, pp. 569–582, 2015.
[49] A. Borji, M.-M. Cheng, H. Jiang, and J. Li, "Salient object detection: A benchmark," *IEEE Trans. Image Process.*, vol. 24, no. 12, pp. 5706–5722, 2015.
[50] D. R. Martin, C. C. Fowlkes, and J. Malik, "Learning to detect natural image boundaries using local brightness, color, and texture cues," *IEEE Trans. Pattern Anal. Mach. Intell.*, vol. 26, no. 5, pp. 530–549, 2004.

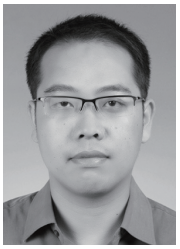

Jing Lou received the BE and ME degrees from Nanjing University of Science and Technology, Nanjing, Jiangsu, P.R. China, where he is currently working toward the PhD degree. His research interests include image processing, computer vision, and machine learning.

Huan Wang received the PhD degree in pattern recognition and intelligent system from Nanjing University of Science and Technology (NUST), Nanjing, Jiangsu, P.R. China. He is currently a lecturer with the School of Computer Science and Engineering, NUST. His current research interests include pattern recognition, robot vision, image processing, and artificial intelligence.

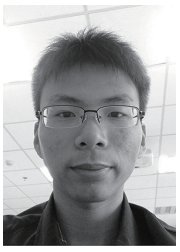

Longtao Chen received the BE degree in computer science and technology from Nanjing University of Science and Technology (NUST), Nanjing, Jiangsu, P.R. China. He is currently working toward the PhD degree in the School of Computer Science and Engineering, NUST. His current research focuses on multi-object tracking.

Qingyuan Xia received the PhD degree in flight vehicle design from Nanjing University of Aeronautics and Astronautics, Nanjing, Jiangsu, P.R. China, in 2013. He is currently a lecturer with the School of Computer Science and Engineering, Nanjing University of Science and Technology, where he worked as a PostDoc from January 2015 to December 2016. His current research interests include environment understanding and navigation technology of intelligent robot, simulation and control of unmanned aerial vehicles.

Wei Zhu received the BE degree in software engineering from Nanjing University of Science and Technology (NUST), Nanjing, Jiangsu, P.R. China. He is currently working toward the PhD degree in the School of Computer Science and Engineering, NUST. His research interests include image processing and deep learning.

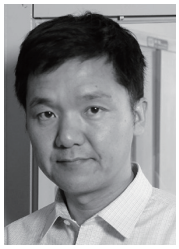

Mingwu Ren received the PhD degree in pattern recognition and intelligent system from Nanjing University of Science and Technology (NUST), Nanjing, Jiangsu, P.R. China, in 2001. He is currently a professor with the School of Computer Science and Engineering, NUST. His current research interests include computer vision, image processing, and pattern recognition.